



**HAL**  
open science

# Apparent diffusion coefficient measured by diffusion MRI of moving and deforming domains

Imen Mekkaoui, Jerome Pousin, Jan Hesthaven, Jing-Rebecca Li

► **To cite this version:**

Imen Mekkaoui, Jerome Pousin, Jan Hesthaven, Jing-Rebecca Li. Apparent diffusion coefficient measured by diffusion MRI of moving and deforming domains. *Journal of Magnetic Resonance*, 2020, 318, pp.106809. 10.1016/j.jmr.2020.106809 . hal-03153152

**HAL Id: hal-03153152**

**<https://hal.science/hal-03153152>**

Submitted on 30 Aug 2022

**HAL** is a multi-disciplinary open access archive for the deposit and dissemination of scientific research documents, whether they are published or not. The documents may come from teaching and research institutions in France or abroad, or from public or private research centers.

L'archive ouverte pluridisciplinaire **HAL**, est destinée au dépôt et à la diffusion de documents scientifiques de niveau recherche, publiés ou non, émanant des établissements d'enseignement et de recherche français ou étrangers, des laboratoires publics ou privés.



Distributed under a Creative Commons Attribution - NonCommercial 4.0 International License

# Apparent diffusion coefficient measured by diffusion MRI of moving and deforming domains

Imen Mekkaoui<sup>a</sup>, Jérôme Pousin<sup>b</sup>, Jan Hesthaven<sup>c</sup>, Jing-Rebecca Li<sup>a,\*</sup>

<sup>a</sup>*INRIA Saclay, Equipe DEFI, CMAP, Ecole Polytechnique, Route de Saclay, 91128 Palaiseau Cedex, France*

<sup>b</sup>*ICJ UMR5208, INSA-Lyon, 20 Av. A. Einstein, 69100 Villeurbanne, France*

<sup>c</sup>*Chair of CMSS, EPFL, Lausanne, Switzerland*

---

## Abstract

The modeling of the diffusion MRI signal from moving and deforming organs such as the heart is challenging due to significant motion and deformation of the imaged medium during the signal acquisition. Recently, a mathematical formulation of the Bloch-Torrey equation, describing the complex transverse magnetization due to diffusion-encoding magnetic field gradients, was developed to account for the motion and deformation. In that work, the motivation was to cancel the effect of the motion and deformation in the MRI image and the space scale of interest spans multiple voxels. In the present work, we adapt the mathematical equation to study the diffusion MRI signal at the much smaller scale of biological cells.

We start with the Bloch-Torrey equation defined on a cell that is moving and deforming and linearize the equation around the magnitude of the diffusion-encoding gradient. The result is a second order signal model in which the linear term gives the imaginary part of the diffusion MRI signal and the quadratic term gives the apparent diffusion coefficient (ADC) attributable to the biological cell. We numerically validate this model for a variety of motions and deformations.

*Keywords:* Diffusion MRI, Bloch-Torrey equation, deforming domain, ADC, finite elements.

---

## 1. Introduction

Diffusion MRI is an imaging modality that is capable of generating images with a contrast that is sensitive to the diffusional motion of water molecules [1]. It plays a very important role in the study of the microscopic structure of biological tissues by measuring the diffusion characteristics of water molecules averaged at the scale of the imaging voxel. While this technique has been very successfully applied to static organs such as the brain [2, 3, 4], the interpretation of the diffusion MRI signal from moving organs like the beating heart is made difficult by the tissue motion and deformation during acquisition. In healthy hearts, the long axes of cardiac myocytes are orientated in a helical arrangement through the ventricular wall and the cardiac cells are organized in laterally

---

\*Corresponding author: [jingrebecca.li@inria.fr](mailto:jingrebecca.li@inria.fr)

10 reinforced layers (sheetlets) of a few cells in thickness [5, 6]. Cardiac diffusion MRI can be used to show angular differences in hypertrophic cardiac myopathy which could be fundamental in assessing heart disease [7, 8, 9]. The sensitivity of diffusion MRI to cardiac motion makes it difficult to assess to what extent the diffusion measurements reflect the real properties of the cardiac tissues. This is illustrated in some experimental studies introduced, for example, in [10, 11, 12, 13, 14, 15].

15 The signal measured in diffusion MRI is the total transverse magnetization in a voxel. This magnetization can be modeled by the complex-valued Bloch-Torrey partial differential equation (PDE) [16]. Originally, this equation was proposed to explain the signal attenuation due to diffusion at the scale of the image, with an (apparent) diffusion coefficient assigned to each voxel. More recently, it has been used to model the transverse magnetization at the microscopic scale, on the scale of the  
20 individual cells. In this way, one can study the contribution to the signal that is attributable to various types of cells or to the extra-cellular space inside the imaging voxel. In static organs, such as the brain, modeling and simulation efforts that link the measured diffusion MRI signal with the geometric structure of the cells and the extra-cellular space include analytical works (see, for example, [17, 18]) and numerical works (see, for example [19, 20, 21, 22, 23, 24, 25]). For the heart, we cite  
25 the works [26, 27, 28, 29, 30] in which *ex-vivo* diffusion MRI is presented by performing numerical simulations on a model of fiber phantom and virtual cardiac microstructure. This model includes a simplified representation of individual cells, with physiologically correct cell size and orientation, and the diffusion MRI is simulated using a Monte Carlo method and realistic MRI sequences. The results are then compared with experimental measurements to validate the proposed model.

30 In contrast to the vast amount of past works for static organs, very few previous modeling and simulation works exist that include the influence of significant physiological motion of the imaged organ during the diffusion MRI acquisition. In [31] the Bloch-Torrey equation is expressed in generalized curvilinear coordinates to describe the behavior of the magnetization in the heart during its deformation over the cardiac cycle and a change of basis formula was used in order to take into  
35 account the effect of motion on diffusion. In another recent work [32], a mathematical formulation of the Bloch-Torrey PDE was developed to account for the motion and deformation. That formulation was obtained by writing the Bloch-Torrey PDE in a domain that deforms over time according to the laws of continuum mechanics and the interest was on cancelling the effect of the motion in the MRI images. In the present work, we adapt the mathematical equations developed in [32] to study  
40 the diffusion MRI signal arising from cells, i.e., the scale of interest will be much smaller than that of the imaging voxel.

In Section 2 we introduce the Bloch-Torrey equation in a moving and deforming biological cell at the microscopic scale. Section 3 is dedicated to the derivation of a new second order model using linearization technique on the solution of the Bloch-Torrey equation. In the new model, the linear  
45 term gives the imaginary part of the diffusion MRI signal and the quadratic term gives the ADC attributable to the biological cell. In Section 4, we present some numerical simulations to validate our model in the presence of an analytical deformation for different geometries of the biological cell. We conclude with some remarks in Section 5.

## 2. Theory

50 Let  $\Omega \subset \mathbb{R}^{dim}$  be the interior of a biological cell (*dim* being the space dimension), and let  $\Gamma = \partial\Omega$  be its boundary. In what follows, we will make the simplifying assumption that the cell membrane

is impermeable. We first describe the Bloch-Torrey PDE in a static cell and then in a moving and deforming cell.

### 2.1. Bloch-Torrey PDE in a biological cell

55 The complex-valued transverse water proton magnetization  $M$  in  $\Omega$  can be described by the following Bloch-Torrey PDE[16]:

$$\begin{cases} \partial_t M(\mathbf{x}, t) - \operatorname{div}_{\mathbf{x}}(\sigma \nabla_{\mathbf{x}} M(\mathbf{x}, t)) + i\gamma \mathbf{g} \cdot \mathbf{x} f(t) M(\mathbf{x}, t) = 0 & \text{in } \Omega \times (0, T) \\ \sigma \nabla M \cdot \mathbf{n}_{\mathbf{x}} = 0 & \text{on } \Gamma \times (0, T) \\ M(\mathbf{x}, 0) = \rho & \text{on } \Omega \times \{0\} \end{cases} \quad (1)$$

where  $\mathbf{n}_{\mathbf{x}}$  is the outward pointing normal to  $\Omega$ ,  $\rho$  is the initial magnetization. The coefficient  $\sigma$  is the intrinsic diffusion coefficient and is assumed constant in  $\Omega$ ,  $\gamma = 2.67513 \times 10^8 \text{ rad s}^{-1} \text{ Tesla}^{-1}$  is the gyro-magnetic ratio of the water proton, and the vector  $\mathbf{g} = g \mathbf{u}_{\mathbf{g}}$  is the applied diffusion-encoding magnetic field gradient ( $g$  containing its magnitude,  $\mathbf{u}_{\mathbf{g}}$  is a unit direction vector in  $\mathbb{R}^{dim}$ ). The function  $f$  is a normalized time profile of the diffusion-encoding magnetic field gradient sequence. The time profile of the standard Pulsed Gradient Spin Echo (PGSE) [17] sequence, simplified to include only the parameters relevant to diffusion, is:

$$f(t) = \begin{cases} 1 & \text{if } 0 < t \leq \delta, \\ -1 & \text{if } \Delta < t \leq \Delta + \delta, \\ 0 & \text{elsewhere.} \end{cases} \quad (2)$$

The time at which the signal is measured is called the echo time  $TE \geq \Delta + \delta$ . The logarithm of the diffusion MRI signal is usually plotted against the b-value:

$$b := \gamma^2 \|\mathbf{g}\|^2 \int_0^{TE} F(t)^2 dt = \gamma^2 \|\mathbf{g}\|^2 \delta^2 \left( \Delta - \frac{\delta}{3} \right),$$

where

$$F(t) = \int_0^t f(s) ds.$$

65 The b-value is an important quantity in diffusion MRI. Typically, for different choices of  $\Delta$  and  $\delta$ , the value of  $\|\mathbf{g}\|$  is adjusted so that the same set of b-values is used.

While physically, the measurable diffusion MRI signal is due to the spins in all the biological cells and the extra-cellular space in a voxel, it makes mathematically sense to define the part of the diffusion MRI signal due to a particular biological cell in order to isolate and study its diffusion characteristics. We define the diffusion MRI signal from the cell  $\Omega$  as the integral of the magnetization at  $TE$  over  $\Omega$ :

$$S = \int_{\Omega} M(\mathbf{x}, TE) d\mathbf{x}.$$

It then follows that the effective diffusion coefficient of the biological cell  $\Omega$  can be defined as:

$$D_{\mathbf{u}_{\mathbf{g}}}^{\text{eff}} \equiv - \frac{1}{\gamma^2 \int_0^{TE} F(t)^2 dt} \frac{\partial}{\partial g^2} \ln \left( \frac{S}{S_0} \right) \Bigg|_{g=0}, \quad (3)$$

where  $S_0$  is the integral of the magnetization over  $\Omega$ , measured for  $g = 0$ . The  $D_{\mathbf{u}_g}^{\text{eff}}$  defined in the formula in Eq.(3) depends on the gradient direction  $\mathbf{u}_g$  and the temporal profile  $f(t)$ , but not on the gradient amplitude  $g$ .

In the MRI community, the effective diffusion coefficient is fitted using the measured diffusion MRI signal at several b-values and the value is referred to as the "apparent diffusion coefficient" (*ADC*). The *ADC* is widely used in medical applications, for instance, *ADC* maps of brain have been used to identify tumors (see [33]).

## 2.2. Moving and deforming biological cell

We consider a moving and deforming biological cell  $\Omega(t) \subset \mathbb{R}^{\dim}$  on the time interval  $t \in [0, T]$  with  $T > 0$ . Let us introduce the geometric transformation  $\varphi$  which is a differentiable, time-space dependent function:

$$\begin{aligned} \varphi : (0, T) \times \Omega(0) &\rightarrow \Omega(t), \\ (t, \mathbf{x}) &\mapsto \varphi(t, \mathbf{x}) = X, \end{aligned}$$

and assume that at each point  $\mathbf{x}$ , the curve  $t \mapsto \varphi(t, \mathbf{x})$  satisfies:

$$\begin{aligned} \partial_t \varphi(t, \mathbf{x}) &= \mathbf{v}(\varphi(t, \mathbf{x}), t), \\ \varphi(0, \mathbf{x}) &= \mathbf{x}, \end{aligned}$$

where  $\mathbf{v}$  is the velocity field  $\mathbf{v} : \mathbb{R}^{\dim} \rightarrow \mathbb{R}^{\dim}$ . In short, the moving and deforming domain  $\{\Omega(t)\}_{t \in [0, T]}$  evolves from the initial domain  $\Omega(0) \subset \mathbb{R}^{\dim}$  according to the transformation  $\varphi$ .

The time variation of the magnetization  $M$  in  $\Omega(t)$  can be written as a function of the diffusion flux through the boundary  $\Gamma(t)$ :

$$\frac{d}{dt} \int_{\Omega(t)} M(X, t) dX = \int_{\Gamma(t)} \sigma \nabla_X M(X, t) \cdot \mathbf{n}_X dS_X.$$

By using the Reynolds transport theorem [34] and taking into account the frequency term ( $i\gamma \mathbf{g} \cdot \mathbf{x} f(t) M(\mathbf{x}, t)$ ) in the Bloch-Torrey PDE in a static domain, we recover the Bloch-Torrey PDE in the moving domain as:

$$\begin{cases} \partial_t M(X, t) - \text{div}_X(\sigma \nabla_X M(X, t)) + \text{div}_X(M(X, t) \mathbf{v}(X, t)) + i\gamma \mathbf{g} \cdot X f(t) M(X, t) = 0 \\ \text{in } \Omega(t) \times (0, T) \\ \sigma \nabla M \cdot \mathbf{n}_X = 0 \quad \text{on } \Gamma(t) \times (0, T) \\ M(X, 0) = \rho(X) \quad \text{on } \Omega(t) \times \{0\}. \end{cases} \quad (4)$$

To transform the magnetization  $M$ , defined on the deforming domain to a related quantity  $\bar{M}$  on the initial domain, we use the definition:

$$\begin{aligned} \bar{M} : \Omega(0) \times (0, T) &\rightarrow \mathbb{R} \\ \bar{M}(\mathbf{x}, t) &\mapsto M(\varphi(t, \mathbf{x}), t). \end{aligned}$$

From [32], under the assumption of the incompressibility of the medium:

$$\text{div}_X(\mathbf{v}) = 0, \quad \det(\mathbf{J}_\varphi) = 1,$$

the Bloch-Torrey PDE for  $\bar{M}$  on  $\Omega(0)$  can be written as:

$$\left\{ \begin{array}{l} \partial_t \bar{M}(\mathbf{x}, t) - \operatorname{div}(\mathbf{J}_\varphi^{-1} \sigma \mathbf{J}_\varphi^{-T} \nabla \bar{M}(\mathbf{x}, t)) + i\gamma \mathbf{g} \cdot \boldsymbol{\varphi}(t, \mathbf{x}) f(t) \bar{M}(\mathbf{x}, t) = 0 \quad \text{in } \Omega(0) \times (0, T), \\ \mathbf{J}_\varphi^{-1} \sigma \mathbf{J}_\varphi^{-T} \nabla \bar{M} \cdot \mathbf{n}_\mathbf{x} = 0 \quad \text{on } \Gamma(0) \times (0, T), \\ \bar{M}(\mathbf{x}, 0) = \rho(\mathbf{x}) \quad \text{on } \Omega(0) \times \{0\}, \end{array} \right\} \quad (5)$$

where  $\mathbf{J}_\varphi = \nabla_{\mathbf{x}} \boldsymbol{\varphi}$  is the Jacobian matrix of the deformation field  $\boldsymbol{\varphi}$ . We use the notation:

$$\mathbf{J}_\varphi^{-T} \equiv (\mathbf{J}_\varphi^{-1})^T.$$

The vector  $\mathbf{n}_\mathbf{x}$  is the outward pointing normal to  $\Omega(0)$ .

In this paper we consider Eq. (5) as the reference model and we refer to it as BTPDE-D (for Bloch-Torrey PDE in a deforming domain), from which we will derive, in the next section, the ADC of a moving and deforming cell. The diffusion MRI signal, obtained by solving Eq. (5), will be called the reference signal:

$$S_{ref} = \int_{\Omega} \bar{M}(\mathbf{x}, TE) d\mathbf{x}. \quad (6)$$

For the details on the derivation of BTPDE-D, the reader is referred to [32].

### 90 3. ADC of BTPDE-D using linearization

In this section we derive the ADC of BTPDE-D using linearization around  $g$ , the magnitude of the diffusion-encoding gradient in (5).

Let us decompose the deformation field as:

$$\boldsymbol{\varphi}(t, \mathbf{x}) := \mathbf{x} + \mathbf{d}(t, \mathbf{x}),$$

where  $\mathbf{d}$  is a displacement field, and we define the Jacobian matrix of  $\boldsymbol{\varphi}$  by:

$$\mathbf{J}_\varphi := \mathbf{I} + \mathbf{J}_\mathbf{d},$$

with  $\mathbf{J}_\mathbf{d} = \nabla_{\mathbf{x}} \mathbf{d}$  being the Jacobian matrix of  $\mathbf{d}$ .

We transform the magnetization  $\bar{M}$  (5) by defining a new unknown  $\widetilde{M}$ :

$$\bar{M}(\mathbf{x}, t) = \widetilde{M}(\mathbf{x}, t) \exp\left(-i\gamma \mathbf{g} \cdot \mathbf{x} \int_0^t f(s) ds\right).$$

It is easy to show that  $\widetilde{M}$  satisfies the following problem:

$$\left\{ \begin{array}{l} \partial_t \widetilde{M}(\mathbf{x}, t) - \operatorname{div}\left(\mathbf{K}(\nabla \widetilde{M}(\mathbf{x}, t) - i\gamma \mathbf{g} F(t) \widetilde{M}(\mathbf{x}, t)) + iF(t) \mathbf{K} \gamma \mathbf{g} \cdot \nabla \widetilde{M}(\mathbf{x}, t), \right. \\ \left. + [\mathbf{K} \gamma \mathbf{g} \cdot \gamma \mathbf{g} F^2(t) + i\gamma \mathbf{g} \cdot \mathbf{d}(t, \mathbf{x}) f(t)] \widetilde{M}(\mathbf{x}, t) = 0 \quad \text{in } \Omega \times (0, T), \right. \\ \left. \mathbf{K}[\nabla \widetilde{M} - i\gamma \mathbf{g} F(t) \widetilde{M}] \cdot \mathbf{n}_\mathbf{x} = 0 \quad \text{on } \Gamma \times (0, T), \right. \\ \left. \widetilde{M}(\mathbf{x}, 0) = \rho \quad \text{on } \Omega \times \{0\}. \right. \end{array} \right\} \quad (7)$$

where

$$\mathbf{K} = \mathbf{J}_\varphi^{-1} \sigma \mathbf{J}_\varphi^{-T}.$$

95 Under the assumption that the initial magnetization  $\rho$  is constant, we introduce a non-dimensional parameter  $\varepsilon > 0$  in  $\mathbf{g}$ , so that  $\mathbf{g} = \varepsilon \tilde{\mathbf{g}}$ . Then (7) becomes:

$$\begin{cases} \partial_t \tilde{M}_\varepsilon(\mathbf{x}, t) - \operatorname{div} \left( \mathbf{K}(\nabla \tilde{M}_\varepsilon(\mathbf{x}, t) - i\varepsilon \gamma \tilde{\mathbf{g}} F(t) \tilde{M}_\varepsilon(\mathbf{x}, t)) + i\varepsilon F(t) \mathbf{K} \gamma \tilde{\mathbf{g}} \cdot \nabla \tilde{M}_\varepsilon(\mathbf{x}, t), \right. \\ \left. + \left[ \varepsilon^2 \mathbf{K} \gamma \tilde{\mathbf{g}} \cdot \gamma \tilde{\mathbf{g}} F^2(t) + i\varepsilon \gamma \tilde{\mathbf{g}} \cdot \mathbf{d}(t, \mathbf{x}) f(t) \right] \tilde{M}_\varepsilon(\mathbf{x}, t) = 0 \quad \text{in } \Omega \times (0, T), \right. \\ \left. \mathbf{K}[\nabla \tilde{M}_\varepsilon - i\varepsilon \gamma \tilde{\mathbf{g}} F(t) \tilde{M}_\varepsilon] \cdot \mathbf{n}_\mathbf{x} = 0 \quad \text{on } \Gamma \times (0, T), \right. \\ \left. \tilde{M}_\varepsilon(\mathbf{x}, 0) = \rho \quad \text{on } \Omega \times \{0\}, \right. \end{cases} \quad (8)$$

Assuming  $\varepsilon$  is small, we write  $\tilde{M}_\varepsilon(\mathbf{x}, t)$  as an expansion in powers of  $\varepsilon$ :

$$\tilde{M}_\varepsilon(\mathbf{x}, t) = \sum_{j=0}^{\infty} \varepsilon^j \tilde{M}_j(\mathbf{x}, t).$$

Inserting the above expansion in (8), we recover the following equations for the first three terms.

– For  $\tilde{M}_0$  :

$$\begin{cases} \partial_t \tilde{M}_0(\mathbf{x}, t) - \operatorname{div}(\mathbf{K} \nabla \tilde{M}_0(\mathbf{x}, t)) = 0 \quad \text{in } \Omega \times (0, T) \\ \mathbf{K} \nabla \tilde{M}_0 \cdot \mathbf{n}_\mathbf{x} = 0 \quad \text{on } \Gamma \times (0, T) \\ \tilde{M}_0(\mathbf{x}, 0) = \rho \quad \text{on } \Omega \times \{0\}. \end{cases} \quad (9)$$

– For  $\tilde{M}_1$  :

$$\begin{cases} \partial_t \tilde{M}_1(\mathbf{x}, t) - \operatorname{div}(\mathbf{K} \nabla \tilde{M}_1(\mathbf{x}, t)) + i \operatorname{div}(\mathbf{K} \gamma \tilde{\mathbf{g}} F(t) \tilde{M}_0(\mathbf{x}, t)) \\ + i F(t) \mathbf{K} \gamma \tilde{\mathbf{g}} \cdot \nabla \tilde{M}_0(\mathbf{x}, t) + i \gamma \tilde{\mathbf{g}} \cdot \mathbf{d}(t, \mathbf{x}) f(t) \tilde{M}_0 = 0 \quad \text{in } \Omega \times (0, T) \\ \mathbf{K}[\nabla \tilde{M}_1 - i \gamma \tilde{\mathbf{g}} F(t) \tilde{M}_0] \cdot \mathbf{n}_\mathbf{x} = 0 \quad \text{on } \Gamma \times (0, T) \\ \tilde{M}_1(\mathbf{x}, 0) = 0 \quad \text{on } \Omega \times \{0\}. \end{cases} \quad (10)$$

100 – For  $\tilde{M}_2$  :

$$\begin{cases} \partial_t \tilde{M}_2(\mathbf{x}, t) - \operatorname{div} \left( \mathbf{K}(\nabla \tilde{M}_2(\mathbf{x}, t) - i \gamma \tilde{\mathbf{g}} F(t) \tilde{M}_1(\mathbf{x}, t)) + i F(t) \mathbf{K} \gamma \tilde{\mathbf{g}} \cdot \nabla \tilde{M}_1(\mathbf{x}, t) + \mathbf{K} \gamma \tilde{\mathbf{g}} \cdot \gamma \tilde{\mathbf{g}} F^2(t) \rho \right. \\ \left. + i \gamma \tilde{\mathbf{g}} \cdot \mathbf{d}(t, \mathbf{x}) f(t) \tilde{M}_1 = 0 \quad \text{in } \Omega \times (0, T) \right. \\ \left. \mathbf{K}[\nabla \tilde{M}_2 - i \gamma \tilde{\mathbf{g}} F(t) \tilde{M}_1] \cdot \mathbf{n}_\mathbf{x} = 0 \quad \text{on } \Gamma \times (0, T) \right. \\ \left. \tilde{M}_2(\mathbf{x}, 0) = 0 \quad \text{on } \Omega \times \{0\}. \right. \end{cases} \quad (11)$$

From (9) we deduce that

$$\tilde{M}_0 \equiv \rho. \quad (12)$$

Consequently (10) is:

$$\begin{cases} \partial_t \tilde{M}_1(\mathbf{x}, t) - \operatorname{div}(\mathbf{K} \nabla \tilde{M}_1(\mathbf{x}, t)) + i \operatorname{div}(\mathbf{K} \gamma \tilde{\mathbf{g}} F(t) \rho) + i \gamma \tilde{\mathbf{g}} \cdot \mathbf{d}(t, \mathbf{x}) f(t) \rho = 0 \quad \text{in } \Omega \times (0, T) \\ \mathbf{K}[\nabla \tilde{M}_1 - i \gamma \tilde{\mathbf{g}} F(t) \rho] \cdot \mathbf{n}_\mathbf{x} = 0 \quad \text{on } \Gamma \times (0, T) \\ \tilde{M}_1(\mathbf{x}, 0) = 0 \quad \text{on } \Omega \times \{0\}. \end{cases} \quad (13)$$

From (13) we observe that  $\widetilde{M}_1$  is purely imaginary, and it can be written as:

$$\widetilde{M}_1 = i\rho\gamma\|\widetilde{\mathbf{g}}\|\omega(\mathbf{x}, t), \quad (14)$$

where  $\omega(\mathbf{x}, t)$  is the solution of:

$$\begin{cases} \partial_t \omega(\mathbf{x}, t) - \operatorname{div}(\mathbf{K}\nabla\omega(\mathbf{x}, t) - F(t)\mathbf{K}\mathbf{u}_{\mathbf{g}}) + \mathbf{u}_{\mathbf{g}} \cdot \mathbf{d}(t, \mathbf{x})f(t) = 0 & \text{in } \Omega \times (0, T) \\ \mathbf{K}[\nabla\omega - F(t)\mathbf{u}_{\mathbf{g}}] \cdot \mathbf{n}_{\mathbf{x}} = 0 & \text{on } \Gamma \times (0, T) \\ \omega(\mathbf{x}, 0) = 0 & \text{on } \Omega \times \{0\}. \end{cases} \quad (15)$$

Equivalently, by defining  $\widetilde{\omega}(\mathbf{x}, t) = \omega(\mathbf{x}, t) - F(t)\mathbf{u}_{\mathbf{g}} \cdot \mathbf{x}$ , we get for  $\widetilde{\omega}$ :

$$\begin{cases} \partial_t \widetilde{\omega}(\mathbf{x}, t) - \operatorname{div}(\mathbf{K}\nabla\widetilde{\omega}(\mathbf{x}, t)) + \mathbf{u}_{\mathbf{g}} \cdot (\mathbf{x} + \mathbf{d}(t, \mathbf{x}))f(t) = 0 & \text{in } \Omega \times (0, T) \\ \mathbf{K}[\nabla\widetilde{\omega}] \cdot \mathbf{n}_{\mathbf{x}} = 0 & \text{on } \Gamma \times (0, T) \\ \widetilde{\omega}(\mathbf{x}, 0) = 0 & \text{on } \Omega \times \{0\}. \end{cases} \quad (16)$$

and

$$\widetilde{M}_1 = i\rho\gamma\|\widetilde{\mathbf{g}}\|(\widetilde{\omega}(\mathbf{x}, t) + F(t)\mathbf{u}_{\mathbf{g}} \cdot \mathbf{x}). \quad (17)$$

After integration in time and space of (11) we recover:

$$\int_{\Omega} \widetilde{M}_2 + i \int_0^t F(s) \int_{\Omega} \mathbf{K}\gamma\widetilde{\mathbf{g}} \cdot \nabla\widetilde{M}_1(\mathbf{x}, s) + \rho \int_0^t F^2(s) \int_{\Omega} \mathbf{K}\gamma\widetilde{\mathbf{g}} \cdot \gamma\widetilde{\mathbf{g}} + i \int_0^t f(s) \int_{\Omega} \gamma\widetilde{\mathbf{g}} \cdot \mathbf{d}(s, \mathbf{x})\widetilde{M}_1 = 0. \quad (18)$$

105 By using the expression of the imaginary part of  $M_1$  (17), (18) becomes:

$$\begin{aligned} \int_{\Omega} \widetilde{M}_2 &= \rho \int_0^t F(s) \int_{\Omega} \mathbf{K}\gamma\widetilde{\mathbf{g}} \cdot \nabla\omega(\mathbf{x}, s)\|\gamma\widetilde{\mathbf{g}}\| - \rho \int_0^t F^2(s) \int_{\Omega} \mathbf{K}\gamma\widetilde{\mathbf{g}} \cdot \gamma\widetilde{\mathbf{g}} \\ &+ \rho \int_0^t f(s) \int_{\Omega} \gamma\widetilde{\mathbf{g}} \cdot \mathbf{d}(s, \mathbf{x})\omega(\mathbf{x}, s)\|\gamma\widetilde{\mathbf{g}}\|. \end{aligned} \quad (19)$$

The transverse magnetization of the biological cell  $\Omega$  to a second order approximation in  $\varepsilon$  is:

$$\widetilde{M}_{\varepsilon} \approx \widetilde{M}_0 + \varepsilon\widetilde{M}_1 + \varepsilon^2\widetilde{M}_2, \quad (20)$$

and the diffusion MRI signal is:

$$S_{new} = \int_{\Omega} (\rho + \varepsilon\widetilde{M}_1(\mathbf{x}, TE) + \varepsilon^2\widetilde{M}_2(\mathbf{x}, TE))d\mathbf{x}.$$

Inserting the expression into the original variable  $\mathbf{g}$  gives the approximation to the signal:

$$\frac{S_{new}}{\rho|\Omega|} = 1 + i\|\gamma\mathbf{g}\|S_{new}^{imag} - ADC_{new}\|\gamma\mathbf{g}\|^2 \int_0^{TE} F(t)^2 dt, \quad (21)$$

where the imaginary part of the signal accounts for the linear term in  $\gamma\mathbf{g}$ :

$$S_{new}^{imag} = \frac{1}{|\Omega|} \int_{\Omega} \omega(\mathbf{x}, TE)d\mathbf{x} = -\frac{1}{|\Omega|} \int_0^{TE} \int_{\Omega} \mathbf{u}_{\mathbf{g}} \cdot \mathbf{d}(t, \mathbf{x})d\mathbf{x}f(t)dt, \quad (22)$$



and the apparent diffusion coefficient (ADC) accounts for the quadratic term in  $\gamma\mathbf{g}$ :

$$ADC_{new} = \frac{1}{|\Omega| \int_0^{TE} F(t)^2 dt} (A_1 + A_2 + A_3), \quad (23)$$

where the three terms that contribute to the ADC are:

$$A_1 = \int_0^{TE} \left( F(t)^2 \int_{\Omega} \mathbf{K}(t, \mathbf{x}) \mathbf{u}_{\mathbf{g}} \cdot \mathbf{u}_{\mathbf{g}} \right) dt, \quad (24)$$

$$A_2 = - \int_0^{TE} \left( F(t) \int_{\Omega} (\mathbf{K}(t, \mathbf{x}) \mathbf{u}_{\mathbf{g}} \cdot \nabla \omega(\mathbf{x}, t)) \right) dt, \quad (25)$$

$$A_3 = - \int_0^{TE} \left( f(t) \int_{\Omega} \mathbf{u}_{\mathbf{g}} \cdot \mathbf{d}(t, \mathbf{x}) \omega(\mathbf{x}, t) \right) dt. \quad (26)$$

Using the divergence theorem for  $A_2$  and the definition of  $\tilde{\omega}$ , we get:

$$\begin{aligned} A_1 + A_2 &= - \int_0^{TE} \left( F(t) \int_{\partial\Omega} \tilde{\omega}(\mathbf{x}, t) \mathbf{K}(t, \mathbf{x}) \mathbf{u}_{\mathbf{g}} \cdot \mathbf{n}_{\mathbf{x}} ds_{\mathbf{x}} \right) dt \\ &\quad + \int_0^{TE} \left( F(t) \int_{\Omega} \tilde{\omega}(\mathbf{x}, t) \operatorname{div}(\mathbf{K}(t, \mathbf{x}) \mathbf{u}_{\mathbf{g}}) d\mathbf{x} \right) dt. \end{aligned}$$

Thus, we can split  $ADC_{new}$  into four terms as follows:

$$ADC_{new} = \frac{1}{|\Omega| \int_0^{TE} F(t)^2 dt} (A_a + A_b + A_c + A_d), \quad (27)$$

where

$$A_a = - \int_0^{TE} \left( F(t) \int_{\partial\Omega} \tilde{\omega}(\mathbf{x}, t) \mathbf{K}(t, \mathbf{x}) \mathbf{u}_{\mathbf{g}} \cdot \mathbf{n}_{\mathbf{x}} ds_{\mathbf{x}} \right) dt \quad (28)$$

$$A_b = - \int_0^{TE} \left( f(t) \int_{\Omega} \mathbf{u}_{\mathbf{g}} \cdot \mathbf{d}(t, \mathbf{x}) \tilde{\omega}(\mathbf{x}, t) d\mathbf{x} \right) dt \quad (29)$$

$$A_c = - \int_0^{TE} \left( f(t) F(t) \int_{\Omega} (\mathbf{u}_{\mathbf{g}} \cdot \mathbf{d}(t, \mathbf{x})) (\mathbf{u}_{\mathbf{g}} \cdot \mathbf{x}) d\mathbf{x} \right) dt \quad (30)$$

$$A_d = \int_0^{TE} \left( F(t) \int_{\Omega} \tilde{\omega}(\mathbf{x}, t) \operatorname{div}(\mathbf{K}(t, \mathbf{x}) \mathbf{u}_{\mathbf{g}}) d\mathbf{x} \right) dt. \quad (31)$$

#### 4. Numerical results

In this section we validate the second order model (21) by comparing it against the reference signal in (6) from the BTPDE-D model.

We design a homogeneous deformation field  $\varphi$  for heart cells (myocytes) given by:

$$\varphi(\mathbf{x}, t) = P(t)\mathbf{x} \quad ; \quad P(t) = \begin{pmatrix} P_{11}(t) & 0 & 0 \\ 0 & P_{22}(t) & 0 \\ 0 & 0 & P_{33}(t) \end{pmatrix} \quad (32)$$

with

$$P_{11}(t) = P_{22}(t) = 1 - V(t), \quad (33)$$

$$P_{33}(t) = 1 + Wk(t), \quad (34)$$

and

$$k(t) = \begin{cases} 0.5(1 - \cos(\pi t/T_s)) & \text{if } t \leq T_s \\ 0.5(1 - \cos(\pi(t-T)/T_d)) & \text{else.} \end{cases}$$

The parameter  $W \geq 0$  controls the amplitude of the deformation,  $T = 1000\text{ms}$  is the duration of one cardiac cycle, where  $T_s = T/3$  is the duration of the contraction of the heart (systolic phase) and  $T_d = 2T/3$  is the duration of dilation (diastolic phase). The function  $V(t)$  is taken in the form:

$$V(t) = 1 - \sqrt{1/P_{33}(t)}. \quad (35)$$

to ensure that

$$\det(P(t)) = 1, \forall t > 0.$$

The displacement field is thus:

$$\mathbf{d}(t, \mathbf{x}) = Q(t)\mathbf{x}, \quad Q(t) = \begin{pmatrix} P_{11}(t) - 1 & 0 & 0 \\ 0 & P_{22}(t) - 1 & 0 \\ 0 & 0 & P_{33}(t) - 1 \end{pmatrix},$$

and the Jacobian matrices, which are independent of  $\mathbf{x}$ , are :

$$\mathbf{J}_\varphi(t) = P(t), \quad \mathbf{J}_\mathbf{d}(t) = Q(t).$$

For this example, the diffusion tensor in the Bloch-Torrey PDE is given by:

$$\mathbf{K}(t) = \sigma(P^{-1}(t))^2.$$

The imaginary part of the signal is

$$S_{new}^{imag} = -\mathbf{u}_g^T \left( \int_0^{TE} Q(t)f(t)dt \right) \left( \frac{1}{|\Omega|} \int_\Omega \mathbf{x}d\mathbf{x} \right), \quad (36)$$

where  $\frac{1}{|\Omega|} \int_\Omega \mathbf{x}d\mathbf{x}$  is the center of mass of the domain. The first term in the ADC is

$$A_a = -\mathbf{u}_g^T \int_0^{TE} F(t)\sigma(Id + Q(t))^{-2} \left( \int_{\partial\Omega} \tilde{\omega}(\mathbf{x}, t)\mathbf{n}_x ds_x \right) dt, \quad (37)$$

where  $\int_{\partial\Omega} \tilde{\omega}(\mathbf{x}, t) \mathbf{n}_{\mathbf{x}} ds_{\mathbf{x}}$  describes the flux of  $\tilde{\omega}(\mathbf{x}, t)$  around the boundary. The second term of the ADC is

$$A_b = -\mathbf{u}_{\mathbf{g}}^T \int_0^{TE} f(t)Q(t) \left( \int_{\Omega} \mathbf{x} \tilde{\omega}(\mathbf{x}, t) d\mathbf{x} \right) dt, \quad (38)$$

where  $\int_{\Omega} \mathbf{x} \tilde{\omega}(\mathbf{x}, t) d\mathbf{x}$  are the moments of  $\tilde{\omega}(\mathbf{x}, t)$  around the principle axes. Finally,

$$A_c = -\mathbf{u}_{\mathbf{g}}^T \left( \int_0^{TE} f(t)F(t)Q(t) dt \right) \left( \int_{\Omega} \mathbf{x} \mathbf{x}^T d\mathbf{x} \right) \mathbf{u}_{\mathbf{g}}, \quad (39)$$

where  $\int_{\Omega} \mathbf{x} \mathbf{x}^T d\mathbf{x}$  are the second order moments of the domain. The last term is independent of the space variable, i.e.:

$$A_d = 0.$$

To study the effects of the geometry we consider a straight cylinder as the canonical geometry of the heart cell as well as two other geometries where the cylinder is twisted and bent, see Figure 1.

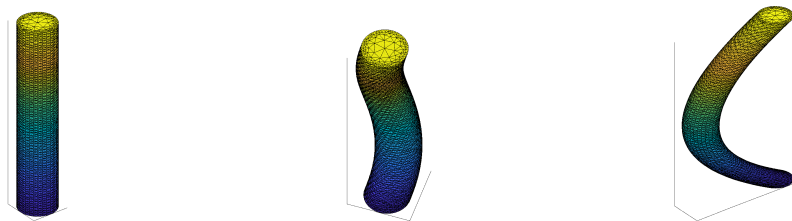


*Figure 1: The finite element-meshes of three cylinders that model a myocyte. The finite-element mesh of the straight cylinder has 13518 nodes and 54921 elements. The finite-element mesh of the twisted cylinder has 13515 nodes and 54883 elements, the bend cylinder has 13530 nodes and 55004 elements.*

The values of  $W$  in the numerical simulations range between 0 and 2. The rate of the deformation is the same in the  $x$  and  $y$  directions. It is a contraction in the first third of  $[0, T]$  (systolic phase) and an extension in the remaining two-thirds (diastolic phase). In the  $z$ -direction, the first third of  $[0, T]$  is an extension and the remaining two-thirds is a contraction. There is no net motion between the starting and ending points of the diffusion MRI experiment over the interval  $[0, T]$ . The effect of the deformation is presented in Figures 2(a), 2(b) and 2(c) for the straight, bent and twisted cylinders at different times in the cardiac cycle.

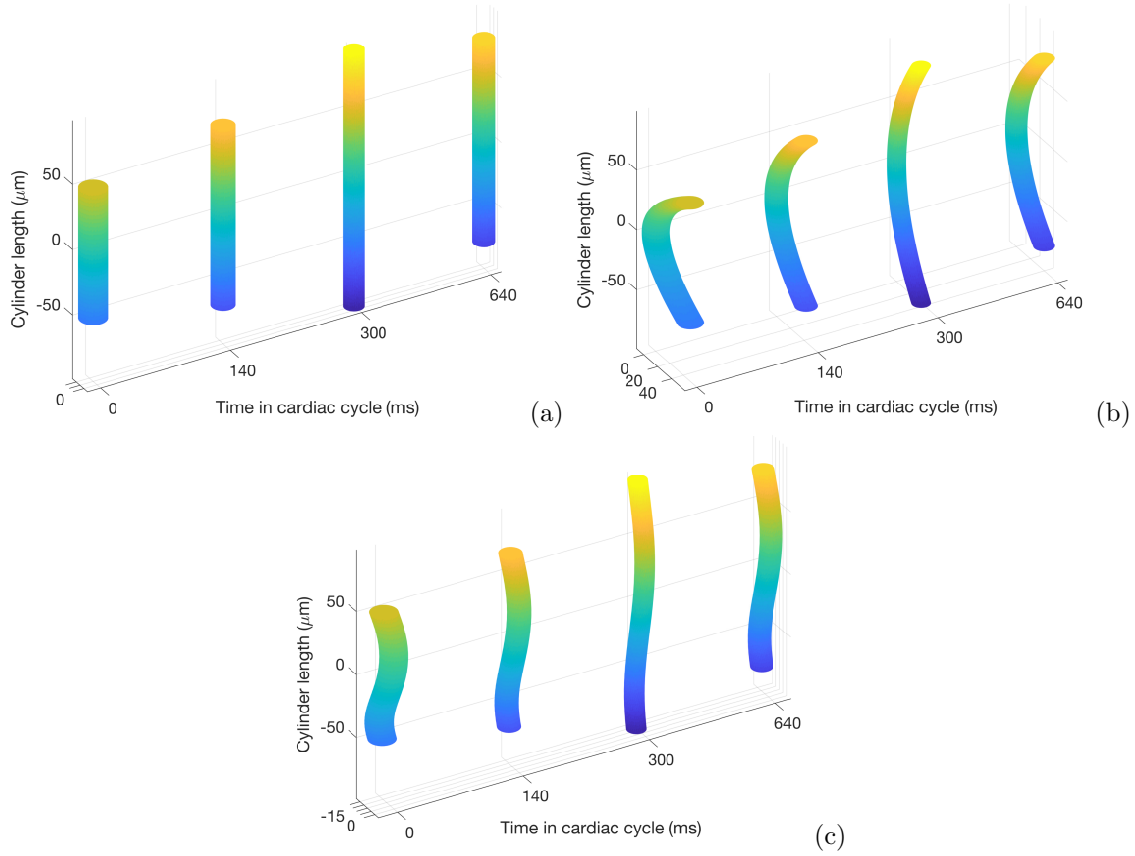


**Figure 2:** *Cylinders at different moments in cardiac deformation. From left to right:  $t=0\text{ms}$ ,  $t=140\text{ms}$  (mid-systole).  $t=300\text{ms}$  (end-systole),  $t=640\text{ms}$  (mid-diastole). Deformation amplitude  $W=1$ . Geometry: (a) straight cylinder. (b) bent cylinder. (c) twisted cylinder.*

We will also simulate a space-dependent deformation field, given by the following equations:

$$P_{33}(t, z) = 1 + Wz^2k(t), \quad (40)$$

$$V(t) = 1 - \sqrt{1/P_{33}(t, z)} \approx \frac{1}{2}Wz^2k(t), \quad (41)$$

$$\begin{aligned} P_{11}(t, z) = P_{22}(t, z) &= 1 - V(t, z), \\ &\approx 1 - \frac{1}{2}Wz^2k(t). \end{aligned} \quad (42)$$

The deformation  $\varphi$  defined as:

$$\varphi(t, \mathbf{x}) = P(t, z)\mathbf{x}$$

with

$$P(t, z) = \begin{pmatrix} P_{11}(t, z) & 0 & 0 \\ 0 & P_{22}(t, z) & 0 \\ 0 & 0 & P_{33}(t, z) \end{pmatrix}$$

will be written as:

$$\varphi(\mathbf{x}, t) = \begin{pmatrix} (1 - \frac{1}{2}Wz^2k(t))x \\ (1 - \frac{1}{2}Wz^2k(t))y \\ (1 + Wz^2k(t))z \end{pmatrix}. \quad (43)$$

#### 4.2. Simulations for one cylindrical cell

In this section we numerically compare the reference signal  $S_{ref}$  in Eq. (6) and the newly derived signal  $S_{new}$  in Eq. (21). We solve (5) to obtain the reference signal and we solve (16) to obtain the new signal. The numerical implementation was done in Matlab using P1 finite elements for the space discretization coupled to the ODE solver "ode23t" for the time integration. The equations were solved on a cylinder of radius  $10\mu m$  and height  $100\mu m$ .

We chose the PGSE sequence [17] with pulse duration  $\delta = 5ms$  and two values of the diffusion time:  $\Delta = 10ms$  and  $\Delta = 40ms$ . The intrinsic diffusion coefficient is chosen as  $\sigma = 2 \times 10^{-3}mm^2/s$ , and the initial condition  $\rho \equiv 1Tesla$ .

For the simulations presented in Figures 3, 4 and 5, 6, 7, we used the homogeneous deformation field (Eqs. (32)–(35)).

In Figure 3 we show the real part of the diffusion MRI signal for  $S_{ref}$  (6) and  $S_{new}$  (21) for two diffusion-encoding directions :  $\mathbf{u}_g = (1, 0, 0)$  and  $\mathbf{u}_g = (0, 0, 1)$ , with  $\delta = 5ms$  and  $\Delta = 40ms$ . We compute the signal during a diffusion sequence at two different points of the cardiac cycle:  $[t, t + TE]$ ,  $t = 140ms$  (mid-systole) and  $t = 640ms$  (mid-diastole). For diffusion in the  $x$ -direction, we observe that the new second order approximation signal is close to the reference signal for all deformation parameter  $W$ , for b-values up to  $500s/mm^2$ , at both time points of the cardiac cycle. However, in the diffusion direction  $z$ ,  $\mathbf{u}_g = (0, 0, 1)$ , the new second order approximation signal is less close to the reference signal for large values of  $W$ , and the inaccuracy is more significant at higher b-values (higher  $g$ ). This is a consequence of our design of the deformation to be more significant in the  $z$ -direction than in the  $x$  and  $y$  directions.

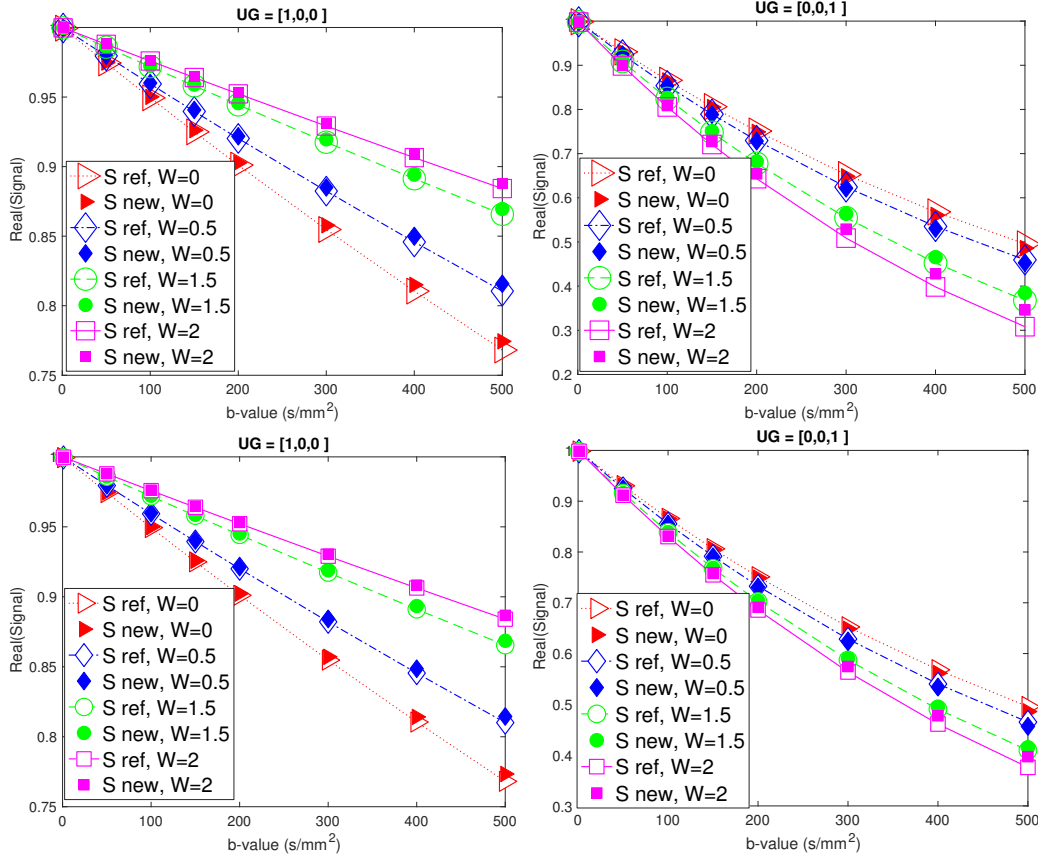


Figure 3: Real part of the reference signal and the new second order approximation signal as a function of  $b$ -value for different values of  $W$ , the deformation parameter ( $W = 0$  means the cell is static during the diffusion MRI sequence). Sequence parameters:  $\delta = 5\text{ms}$  and  $\Delta = 40\text{ms}$ . Top left:  $t=140\text{ms}$  (mid-systole),  $\mathbf{u}_g = (1, 0, 0)$ . Top right:  $t=140\text{ms}$  (mid-systole),  $\mathbf{u}_g = (0, 0, 1)$ . Bottom left:  $t=640\text{ms}$  (mid-diastole),  $\mathbf{u}_g = (1, 0, 0)$ . Bottom right:  $t=640\text{ms}$  (mid-diastole),  $\mathbf{u}_g = (0, 0, 1)$ . Geometry: straight cylinder. Deformation field: Homogeneous (Eqs.(32)–(35)).

In Figure 4 we show the imaginary part of the new second order approximation signal,  $S_{new}^{imag}$ , for diffusion encoding in the  $x$ -direction,  $\mathbf{u}_g = (1, 0, 0)$ , at  $t=140\text{ms}$  (mid-systole) in the cardiac cycle. Due to the presence of cardiac deformation ( $W \neq 0$ ), the imaginary part of the signal is non-zero, unlike the case without deformation ( $W = 0$ ).

145

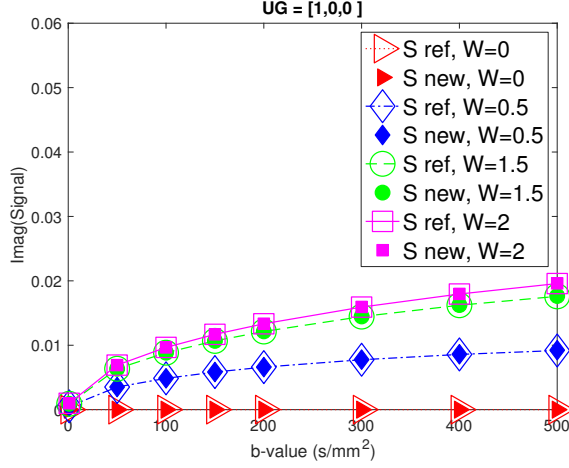


Figure 4: Imaginary part of the reference signal and the new second order approximation signal as a function of b-value for different values of the deformation parameter  $W$  ( $W = 0$  means the cell is static during the diffusion MRI sequence),  $t = 140\text{ms}$  (mid-systole) of the cardiac cycle. Sequence parameters:  $\delta = 5\text{ms}$  and  $\Delta = 40\text{ms}$ . Geometry: straight cylinder. Deformation field: Homogeneous (Eqs.(32)–(35)).

Next, we compare the reference  $ADC_{ref}$  (3) and the newly derived  $ADC_{new}$  (27), both normalized by dividing by the intrinsic diffusion coefficient  $\sigma$ . In Figure 5, we show the normalized ADCs in two diffusion-encoding directions:  $\mathbf{u}_g = (1, 0, 0)$  and  $\mathbf{u}_g = (0, 0, 1)$ , at several different time points in the cardiac cycle:  $t = \{140, 300, 640\}\text{ms}$ , for two diffusion-encoding sequences: PGSE ( $\delta = 5\text{ms}$ ,  $\Delta = 10\text{ms}$ ) and PGSE ( $\delta = 5\text{ms}$ ,  $\Delta = 40\text{ms}$ ). It can be seen that the ADC of the new second order approximation signal model is very accurate for describing the ADC of the reference model.

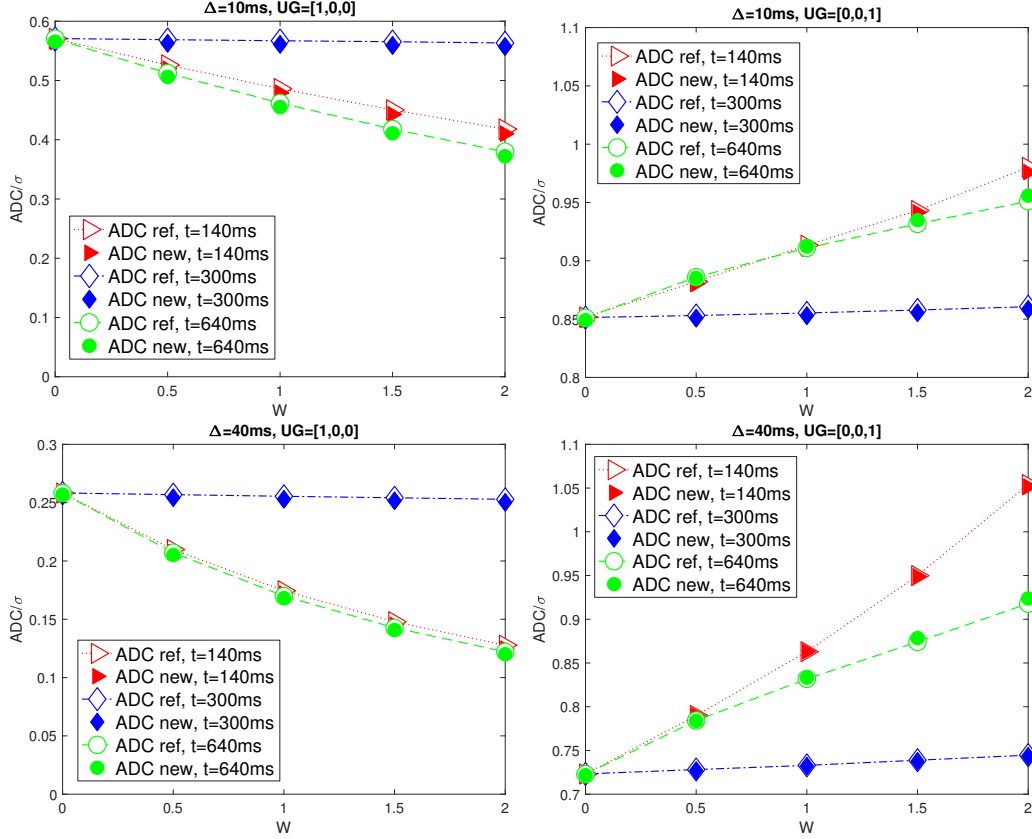


Figure 5: The normalized ADC of the reference signal and the ADC of the new second order approximation signal as function of the deformation parameter  $W$  ( $W = 0$  means the cell is static during the diffusion MRI sequence), at different time points in the cardiac cycle:  $t=140, 300, 640ms$ . Top left, PGSE ( $\delta = 5ms, \Delta = 10ms$ ),  $\mathbf{u}_g = (1, 0, 0)$ . Top right, PGSE ( $\delta = 5ms, \Delta = 10ms$ ),  $\mathbf{u}_g = (0, 0, 1)$ . Bottom left, PGSE ( $\delta = 5ms, \Delta = 40ms$ ),  $\mathbf{u}_g = (1, 0, 0)$ . Bottom right, PGSE ( $\delta = 5ms, \Delta = 40ms$ ),  $\mathbf{u}_g = (0, 0, 1)$ . Geometry: straight cylinder. Deformation field: Homogeneous (Eqs.(32)–(35)).

In Figure 6, we show the normalized ADC of the new second order approximation signal model (27), computed in 800 directions, uniformly distributed in the unit sphere, for the sequence PGSE ( $\delta = 5ms, \Delta = 40ms$ ). The results are presented for the deformation amplitude  $W=0$  (without deformation effect) and  $W = 1, W = 2$ . The ADC is computed for different time points in the cardiac cycle:  $t = \{140, 300, 640\}ms$ . As in Figure 5 we see that the ADC without cardiac deformation ( $W = 0$ ) coincides with the one at the end of the systolic phase ( $t = 300ms$ ) because in that moment the time variation of the heart deformation is negligible. This confirms the simulation results obtained in [35] and the experimental results in [10]. To show the effect of the deformation amplitude  $W$ , we compare the ADC at  $t=140ms$  and  $t=640ms$  of the cardiac cycle for  $W = 1$  and  $W = 2$ . We see clearly that the larger  $W$  induces a larger ADC in the  $z$  direction. This effect is minimal in the  $x$  and  $y$  diffusion-encoding directions.



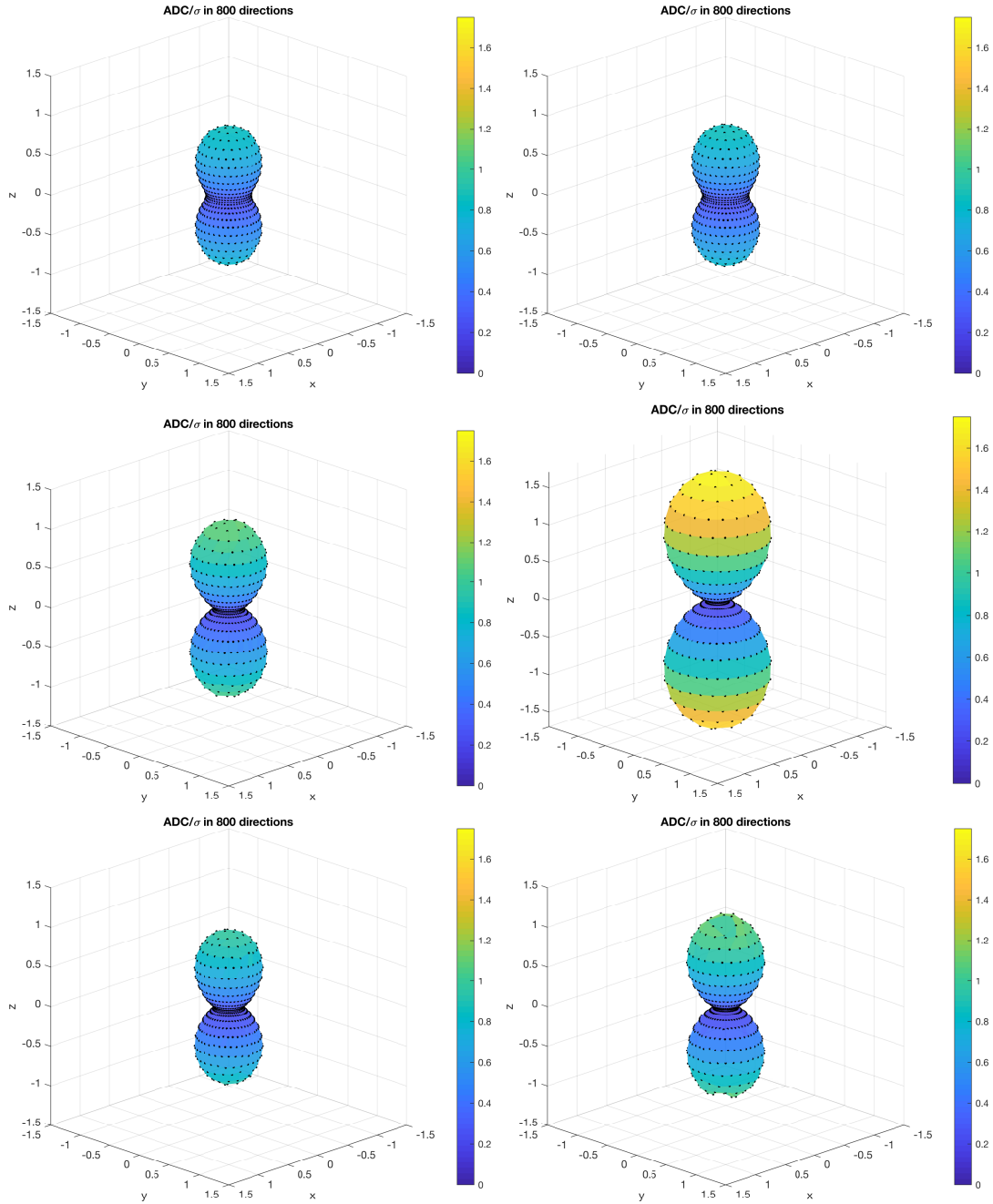


Figure 6: Normalized ADC of the new second order approximation signal model (27), computed in 800 directions, uniformly distributed in the unit sphere, for the sequence PGSE ( $\delta = 5\text{ms}$ ,  $\Delta = 40\text{ms}$ ),  $W$  is the deformation parameter,  $t$  indicates the point in the cardiac cycle. Top left:  $W=0$  (no deformation). Top right:  $W=1$ ,  $t=300\text{ms}$ . Middle left:  $W=1$ ,  $t=140\text{ms}$ . Middle right:  $W=2$ ,  $t=140\text{ms}$ . Bottom left:  $W=1$ ,  $t=640\text{ms}$ . Bottom right:  $W=2$ ,  $t=640\text{ms}$ . The black points are the magnitude of the normalized ADC multiplied by the diffusion-encoding direction. The color indicates the value of the normalized ADC. Geometry: straight cylinder. Deformation field: Homogeneous (Eqs.(32)–(35)).

In Figure 7 we show the effect of the shape of the cylindrical cell on the ADC. We compute  
165 the normalized ADC of the new second order approximation signal model (27), in 800 directions,  
uniformly distributed on the unit sphere, for the sequence PGSE ( $\delta = 5\text{ms}$ ,  $\Delta = 40\text{ms}$ ) for the bent  
cylinder (Figure 2(b)) and the twisted cylinder (Figure 2(c)). Again, we observe that the ADC  
without cardiac deformation ( $W = 0$ ) coincides with the one at the end systolic phase ( $t = 300\text{ms}$ )  
170 when the variation of the heart deformation during the application of the diffusion encoding sequence  
is negligible.

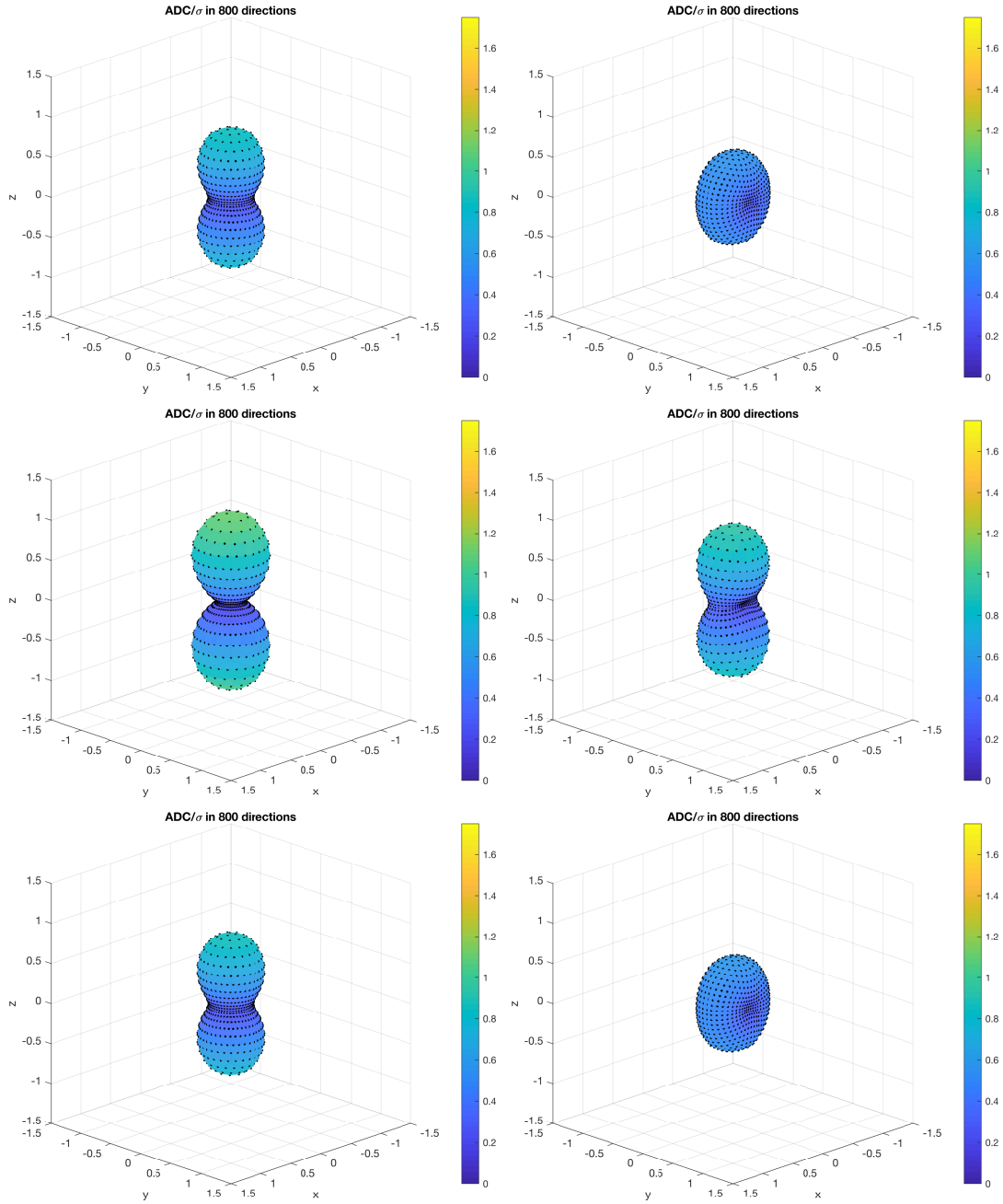


Figure 7: Normalized ADC of the new second order approximation signal model (27), computed in 800 directions, uniformly distributed in the unit sphere, for the sequence PGSE ( $\delta = 5\text{ms}$ ,  $\Delta = 40\text{ms}$ ). The black points are the magnitude of the normalized ADC multiplied by the diffusion-encoding direction. The color indicates the value of the normalized ADC.  $W$  is the deformation parameter,  $t$  indicates the point in the cardiac cycle. Top left: twisted cylinder,  $W = 0$  (no deformation effect). Top right: bend cylinder,  $W = 0$  (no deformation effect). Middle left: twisted cylinder,  $W = 1$  and  $t = 140\text{ms}$ . Middle right: bend cylinder,  $W = 1$  and  $t = 140\text{ms}$ . Bottom left: twisted cylinder,  $W = 1$  and  $t = 300\text{ms}$ . Bottom right: bend cylinder,  $W = 1$  and  $t = 300\text{ms}$ . Deformation field: Homogeneous (Eqs.(32)–(35)).

We see that the ADC for the twisted cylinder and the straight cylinder are similar, whereas the ADC of the bent cylinder is significantly different. To explain this phenomenon, we show the differences in the directional surface to volume ratios of these 3 geometries. The directional surface to volume ratio comes up in the well-known formula for the ADC in the short diffusion time regime. The short time approximation (STA) [36, 37] formula is the following (with correction for non-narrow pulses [38]):

$$STA = \sigma \left[ 1 - \frac{4\sqrt{\sigma}}{3\sqrt{\pi}} C_{\delta,\Delta} \frac{A_{\mathbf{u}_g}}{V} \right], \quad (44)$$

with  $\sigma$  being the intrinsic diffusivity coefficient, and

$$A_{\mathbf{u}_g} = \int_{\partial\Omega} (\mathbf{u}_g \cdot \mathbf{n})^2 ds$$

is the gradient direction dependent surface area, the pulse separation and pulse duration are accounted for by:

$$C_{\delta,\Delta} = \frac{4}{35} \frac{(\Delta + \delta)^{7/2} + (\Delta - \delta)^{7/2} - 2(\delta^{7/2} + \Delta^{7/2})}{\delta^2(\Delta - \delta/3)} = \sqrt{\Delta} \left( 1 + \frac{1}{3} \frac{\delta}{\Delta} - \frac{8}{35} \left( \frac{\delta}{\Delta} \right)^{3/2} + \dots \right).$$

When  $\delta \ll \Delta$ , the value  $C_{\delta,\Delta}$  is approximately  $\sqrt{\Delta}$ .

In Figure 8, we show the ADC obtained by evaluating the above STA formula. It is clear that the STA formula closely tracks the shapes of the ADC shown in Figures 6 and 7. There is a minor difference in the case of the bend cylinder when  $W = 0$  (the sphere being flat along the  $z$ -axis rather than the  $y$ -axis), but clearly, the directional surface area of the bend cylinder is significantly different than those of the straight and twist cylinders.

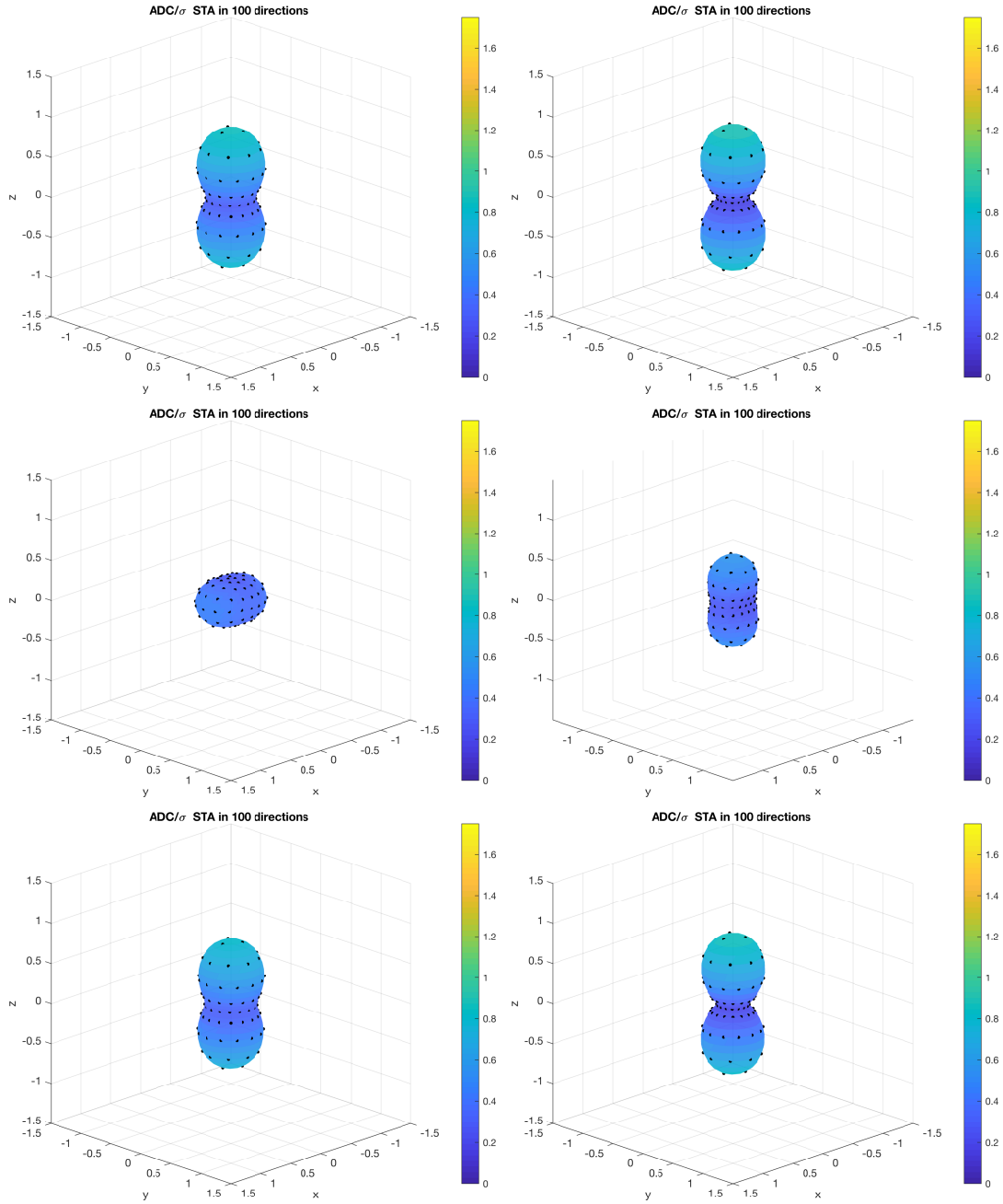


Figure 8: Normalized ADC in the short time approximation regime (STA), computed in 100 directions, uniformly distributed in the unit sphere, for the sequence PGSE ( $\delta = 5\text{ms}$ ,  $\Delta = 40\text{ms}$ ). The black points are the magnitude of the normalized ADC multiplied by the diffusion-encoding direction. The color indicates the value of the normalized ADC.  $W$  is the deformation parameter,  $t$  indicates the point in the cardiac cycle. Top left: straight cylinder,  $W = 0$  (no deformation effect). Top right: straight cylinder,  $W = 1$ ,  $t=140\text{ms}$ . Middle left: bend cylinder,  $W = 0$ . Middle right: bend cylinder,  $W = 1$ ,  $t = 140\text{ms}$ . Bottom left: twisted cylinder,  $W = 0$ . Bottom right: twisted cylinder,  $W = 1$ ,  $t = 140\text{ms}$ . Deformation field: Homogeneous (Eqs.(32)–(35)).

Now we show simulation results of the non-homogeneous deformation field (Eqs. (40)–(43)). In Figure 9, we can see that, similar to the homogeneous deformation field we showed previously, the higher signal curves in the  $x$ -direction are due to a more deformed field (higher  $W$ ), and in the  $z$ -direction, they are due to a less deformed field (lower  $W$ ). Also similar to the homogeneous deformation field, the ADC in Figure 10 at time  $t=300\text{ms}$  for non-zero values of  $W$  is approximately the same as for  $W = 0$ . However, some differences can be seen between the two deformation fields. For example, in the  $z$ -direction, the differences at larger  $W$  between the ADC at  $t=140\text{ms}$  and the ADC at  $t=640\text{ms}$  are smaller for the non-homogeneous deformation field than for the homogeneous one. This difference can be seen also in Figure 11, where we show the magnetization solution at TE for the straight cylinder undergoing the two deformations. For the homogeneous deformation field, the difference in the magnetization solution between  $t=140\text{ms}$  and  $t = 640\text{ms}$  are more significant than for the case of the non-homogeneous deformation field.

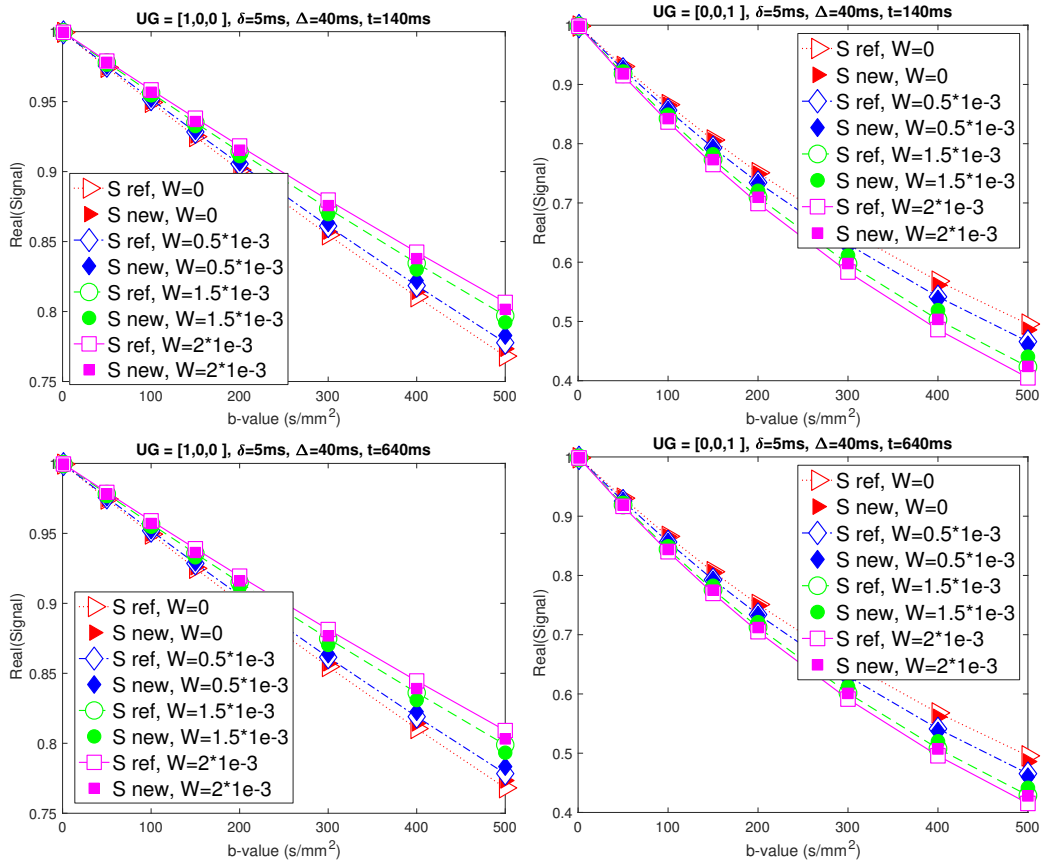


Figure 9: Real part of the reference signal and the new second order approximation signal as a function of  $b$ -value for different values of  $W$ , the deformation parameter ( $W = 0$  means the cell is static during the diffusion MRI sequence). Sequence parameters:  $\delta = 5\text{ms}$  and  $\Delta = 40\text{ms}$ . Top left:  $t=140\text{ms}$  (mid-systole),  $\mathbf{u}_g = (1, 0, 0)$ . Top right:  $t=140\text{ms}$  (mid-systole),  $\mathbf{u}_g = (0, 0, 1)$ . Bottom left:  $t=640\text{ms}$  (mid-diastole),  $\mathbf{u}_g = (1, 0, 0)$ . Bottom right:  $t=640\text{ms}$  (mid-diastole),  $\mathbf{u}_g = (0, 0, 1)$ . Geometry: straight cylinder. Deformation field: Non-homogeneous (Eqs. (40)–(43)).

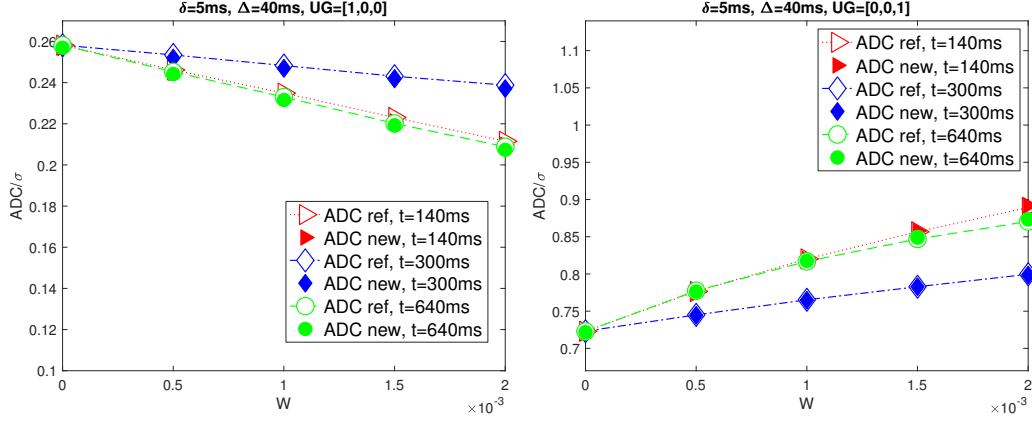


Figure 10: The normalized ADC of the reference signal and the ADC of the new second order approximation signal as function of the deformation parameter  $W$  ( $W = 0$  means the cell is static during the diffusion MRI sequence), at different time points in the cardiac cycle:  $t=140, 300, 640\text{ms}$ . Left, PGSE ( $\delta = 5\text{ms}$ ,  $\Delta = 40\text{ms}$ ),  $\mathbf{u}_g = (1, 0, 0)$ . Right, PGSE ( $\delta = 5\text{ms}$ ,  $\Delta = 40\text{ms}$ ),  $\mathbf{u}_g = (0, 0, 1)$ . Geometry: straight cylinder. Deformation field: Non-homogeneous (Eqs. (40)–(43)).

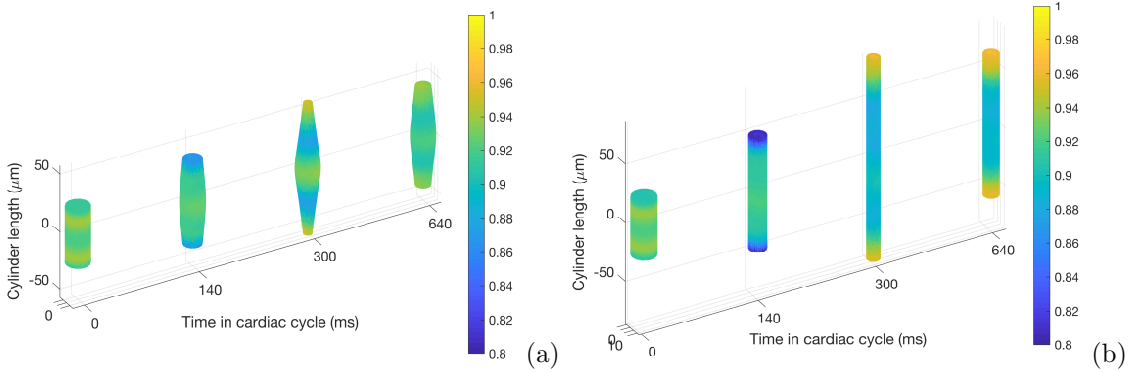


Figure 11: Magnetization solution of Eq. (5) at echo time (TE) for  $\delta = 5\text{ms}$ ,  $\Delta = 40\text{ms}$ ,  $\mathbf{u}_g = (0, 0, 1)$  and  $b\text{-value}=50\text{s/mm}^2$ . Moments of the cardiac cycle: From left to right:  $t=0\text{ms}$ ,  $t=140\text{ms}$  (mid-systole),  $t=300\text{ms}$  (end-systole),  $t=640\text{ms}$  (mid-diastole). Geometry: straight cylinder. (a) Non-homogeneous deformation field (Eqs. (40)–(43)). Deformation amplitude  $W=2 \times 10^{-3}$ . (b) Homogeneous deformation field (Eqs.(32)–(35)). Deformation amplitude  $W=2$ .

### 4.3. Computational time

190 In Table 1 we show the computational times for the simulation of the reference model (BTPDE-D) and the new second order approximation model for the straight cylinder. All the simulations were performed on a server computer with 12 processors (Intel (R) Xeon (R) E5-2667 @2.90 GHz), 192 GB of RAM, running CentOS 7, using MATLAB R2019a. It can be seen that the new second order model takes about 70% of the computational time of the reference model. In Table 2 we show  
 195 the computational times to simulate the new second order model for the twisted and bend cylinders. The computational times do not depend on the value of the deformation parameter  $W$  and on the

point of the cardiac cycle simulated. These computational times are provided to illustrate typical simulation times. Though the advantages of the new second order model include shorter simulation times, more significant advantages lie in the fact that it is more amenable to mathematical analysis.

	Reference model (BTPDE-D)	New 2nd order model
$\delta = 5\text{ms}, \Delta = 10\text{ms}$	71.62 sec	47.99 sec
$\delta = 5\text{ms}, \Delta = 40\text{ms}$	72.53 sec	51.04 sec

*Table 1: The average computational times to obtain the ADC, per diffusion-encoding direction. Geometry: straight cylinder (13518 nodes and 54921 elements).*

Finite-element mesh size	New 2nd order model
Twisted cylinder Nodes: 13515, Elements: 54883	57.5 sec
Bend cylinder Nodes: 13530, Elements: 55004	55.1 sec

*Table 2: The computational times to obtain the new 2nd order model, per diffusion-encoding direction. The sequence is PGSE ( $\delta = 5\text{ms}$ ,  $\Delta = 40\text{ms}$ ).*

## 200 5. Concluding remarks

We derived a second order (in the diffusion-encoding gradient magnitude  $g$ ) signal perturbation model whose linear term gives the imaginary part of the diffusion MRI signal and whose quadratic term gives the ADC attributable to the biological cell. We numerically validated this model for a constructed example of cardiac motion and deformation using a finite element discretization of the equations in a cylindrical cell.

This work is a first step to understand the origins of the imaginary part of the diffusion MRI signal in the case of moving and deforming domains and the deviation of the ADC from that which is measured in the case of a static domain. By formulating the second order model, we are able to write the different contributing factors to the linear and the quadratic terms in (21). In particular, we related the imaginary part of the signal to the center of mass of the domain (22) and the ADC to four contributing terms (27). We gave a physical interpretation to these contributing factors in terms of the flux and the moments of the function  $\tilde{\omega}(\mathbf{x}, t)$ . The next step is to understand  $\tilde{\omega}(\mathbf{x}, t)$ , which is a solution of a diffusive PDE subject to zero initial conditions and homogeneous Neumann boundary conditions.

In addition to providing an analytic understanding of the diffusion MRI of moving and deforming domains, our work also included the implementation of a numerical method to simulate the BTPDE-D model and the new second order approximation signal model.



## Acknowledgement

220 The authors gratefully acknowledge the *Inria International Lab (IIL) Inria-EPFL* for financially  
225 supporting the post-doc of Imen Mekkaoui during which the work presented in this paper was  
performed.

## References

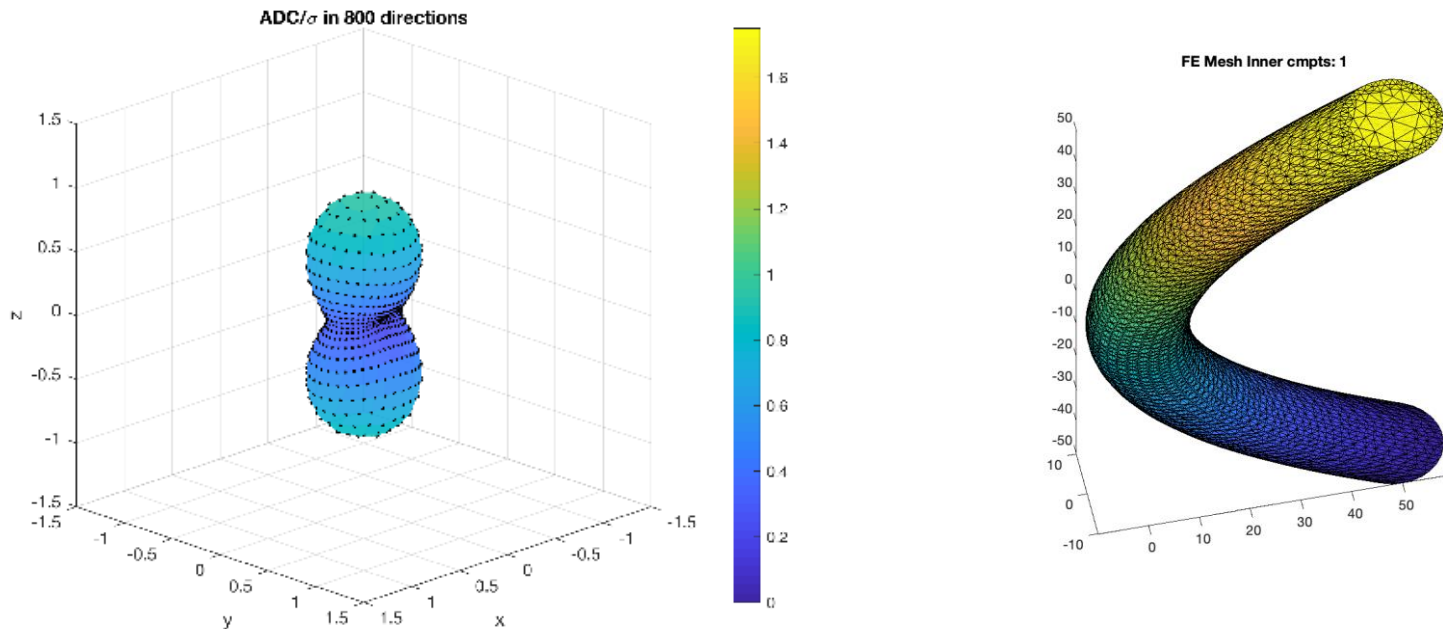
- [1] Denis Le Bihan and E. Breton. Imagerie de diffusion in-vivo par résonance magnétique  
225 nucléaire. Comptes-Rendus de l'Académie des Sciences, 93(5):27–34, 1985.
- [2] Mark A. Horsfield and Derek K. Jones. Applications of diffusion-weighted and diffusion tensor  
mri to white matter diseases - a review. NMR in Biomedicine, 15(7–8):570–577, 2002.
- [3] S. Warach, D. Chien, W. Li, M. Ronthal, and R. R. Edelman. Fast magnetic resonance  
diffusion-weighted imaging of acute human stroke. Neurology, 42(9):1717–1717, 1992.
- 230 [4] Mariana Lazar. Mapping brain anatomical connectivity using white matter tractography. NMR  
in Biomedicine, 23(7):821–835, 2010.
- [5] D. Streeter, H. M. Spotnitz, D. P. Patel, J. Ross, and E. H. Sonnenblick. Fiber orientation in  
the canine left ventricle during diastole and systole. Circuit Res, 24(3):339–347.
- 235 [6] Alfonso Bueno-Orovio, Irvin Teh, Jurgen Schneider, Kevin Burrage, and Vicente Grau. Anoma-  
lous diffusion in cardiac tissue as an index of myocardial microstructure. IEEE Transactions  
on Medical Imaging, 35:2200–2207, 05 2016.
- [7] L Garrido, V J Wedeen, K K Kwong, U M Spencer, and H L Kantor. Anisotropy of water  
diffusion in the myocardium of the rat. Circulation Research, 74(5):789–793, 1994.
- 240 [8] Laura-Ann McGill Sonia Nielles-Vallespin Andrew D Scott Siew Y Ho Karen P McCarthy  
Margarita M Haba Tevfik F Ismail Peter D Gatehouse Ranil de Silva Alexander R Lyon  
Sanjay K Prasad David N Firmin Pedro F Ferreira, Philip J Kilner and Dudley J Pennell. In  
vivo cardiovascular magnetic resonance diffusion tensor imaging shows evidence of abnormal  
myocardial laminar orientations and mobility in hypertrophic cardiomyopathy. Journal of  
Cardiovascular Magnetic Resonance, 16(87), 2014.
- 245 [9] Matt G. Hall and Chris A. Clark. Diffusion in hierarchical systems: A simulation study in  
models of healthy and diseased muscle tissue. Magnetic Resonance in Medicine, 78(3):1187–  
1198, 2017.
- [10] Stanislas Rapacchi, Han Wen, Magalie Viallon, Denis Grenier, Peter Kellman, Pierre Croisille,  
and Vinay M Pai. Low b-value diffusion-weighted cardiac magnetic resonance imaging: initial  
250 results in humans using an optimal time-window imaging approach. Investigative radiology,  
46(12):751 – 758, 2011.
- [11] Timothy G. Reese, Robert M. Weisskoff, R. Neil Smith, Bruce R. Rosen, Robert E. Dinsmore,  
and Van J. Wedeen. Imaging myocardial fiber architecture in vivo with magnetic resonance.  
Magnetic Resonance in Medicine, 34(6):786–791, 1995.

- 255 [12] Jiangang Dou, Timothy G. Reese, Wen-Yih I. Tseng, and Van J. Wedeen. Cardiac diffusion mri without motion effects. Magnetic Resonance in Medicine, 48(1):105–114, 2002.
- [13] Urs Gamper, Peter Boesiger, and Sebastian Kozerke. Diffusion imaging of the in vivo heart using spin echoes-considerations on bulk motion sensitivity. Magnetic Resonance in Medicine, 57(2):331–337, 2007.
- 260 [14] TG Reese, VJ Wedeen, and RM Weisskoff. Measuring diffusion in the presence of material strain. Journal of magnetic resonance. Series B, 112:253–8, 1996.
- [15] Christian Stoeck, Aleksandra Kalinowska, Constantin von Deuster, Jack Harmer, Rachel W Chan, Markus Niemann, Robert Manka, David Atkinson, David E Sosnovik, Choukri Mekkaoui, and Sebastian Kozerke. Dual-phase cardiac diffusion tensor imaging with strain correction. PloS one, 9:e107159, 2014.
- 265 [16] H.C. Torrey. Bloch equations with diffusion terms. Physical Review, 104:563–565, 1956.
- [17] E.O. Stejskal and J.E. Tanner. Spin diffusion measurements: Spin echoes in the presence of a time-dependent field gradient. JCP, 42:288–292, 1965.
- [18] Josef Pfeuffer, Ulrich Flögel, Wolfgang Dreher, and Dieter Leibfritz. Restricted diffusion and exchange of intracellular water: Theoretical modelling and diffusion time dependence of 1h nmr measurements on perfused glial cells. NMR in biomedicine, 11:19–31, 1998.
- 270 [19] Junzhong Xu, Mark D Does, and John C Gore. Numerical study of water diffusion in biological tissues using an improved finite difference method. Physics in Medicine & Biology, 52(7):N111, 2007.
- 275 [20] Benjamin F. Moroney, Timothy Stait-Gardner, Bahman Ghadirian, Nirbhay N. Yadav, and William S. Price. Numerical analysis of nmr diffusion measurements in the short gradient pulse limit. Journal of Magnetic Resonance, 234:165 – 175, 2013.
- [21] Dang Van Nguyen, Jing-Rebecca Li, Denis Grebenkov, and Denis Le Bihan. A finite elements method to solve the bloch–torrey equation applied to diffusion magnetic resonance imaging. Journal of Computational Physics, 263:283 – 302, 2014.
- 280 [22] Jing-Rebecca Li, Hang Tuan Nguyen, Dang Van Nguyen, Housseem Haddar, Julien Coatléven, and Denis Le Bihan. Numerical study of a macroscopic finite pulse model of the diffusion mri signal. Journal of Magnetic Resonance, 248:54 – 65, 2014.
- [23] Julien Coatléven, Housseem Haddar, and Jing-Rebecca Li. A macroscopic model including membrane exchange for diffusion mri. SIAM Journal on Applied Mathematics, 74(2):516–546, 2014.
- 285 [24] Housseem Haddar, Jing-Rebecca Li, and Simona Schiavi. A macroscopic model for the diffusion mri signal accounting for time-dependent diffusivity. SIAM Journal on Applied Mathematics, 76(3):930–949, 2016.
- 290 [25] Housseem Haddar, Marwa Kchaou, and Maher Moakher. The derivation of homogenized diffusion kurtosis models for diffusion mri. Journal of Magnetic Resonance, 298:48 – 57, 2019.

- 295 [26] Els Fieremans, Yves De Deene, Steven Delputte, Mahir S. Azdimir, Yves DaAsseler, Jelle Vlassenbroeck, Karel Deblaere, Eric Achten, and Ignace Lemahieu. Simulation and experimental verification of the diffusion in an anisotropic fiber phantom. Journal of Magnetic Resonance, 190(2):189 – 199, 2008.
- [27] Lihui Wang, Yuemin Zhu, Hongying Li, Wanyu Liu, and Isabelle Magnin. Simulation of diffusion anisotropy in dti for virtual cardiac fiber structure. volume 6666, pages 95–104, 2011.
- 300 [28] L. Wang, Y. Zhu, H. Li, W. Liu, and a. I. E. Magnin. Multi-scale modeling and simulation of the cardiac fiber architecture for dmri. IEEE Transactions on Biomedical Engineering, 59(1):16–19, 2012.
- [29] L. Wang, Y. Zhu, F. Yang, W. Liu, and I. E. Magnin. Simulation of dynamic dti of 3d cardiac fiber structures. In 2014 IEEE 11th International Symposium on Biomedical Imaging (ISBI), pages 714–717, 2014.
- 305 [30] J. Bates, I. Teh, D. McClymont, P. Kohl, J. E. Schneider, and V. Grau. Monte carlo simulations of diffusion weighted mri in moycardium: Validation and sensitivity analysis. IEEE Transactions on Medical Imaging, 36(6):1316–1325, 2017.
- [31] D. Rohmer and G.T. Gullberg. A bloch-torrey equation for diffusion in a deforming media. Technical report, University of California, 2006.
- 310 [32] Elie Bretin, Imen Mekkaoui, and Jérôme Pousin. Assessment of the effect of tissue motion in diffusion mri: Derivation of new apparent diffusion coefficient formula. Inverse Problems & Imaging, 12:125, 2018.
- [33] R-V. Mulkern S-E. Maier, Y. Sun. Diffusion imaging of brain tumors. NMR Biomed., 23(7):849–864, 2010.
- 315 [34] Stephen Bechtel and Robert Lowe. Fundamentals of Continuum Mechanics: With Applications to Mechanical, Thermomechanical, and Smart Materials. Academic Press, 2014.
- [35] I. Mekkaoui, K. Moulin, P. Croisille, J. Pousin, and M. Viallon. Quantifying the effect of tissue deformation on diffusion-weighted mri: A mathematical model and an efficient simulation framework applied to cardiac diffusion imaging. Physics in Medicine and Biology, 61:5662–5686, 2016.
- 320 [36] Partha P Mitra, Pabitra N Sen, Lawrence M Schwartz, and Pierre Le Doussal. Diffusion propagator as a probe of the structure of porous media. Physical review letters, 68(24):3555–3558, 1992.
- 325 [37] Partha P. Mitra, Pabitra N. Sen, and Lawrence M. Schwartz. Short-time behavior of the diffusion coefficient as a geometrical probe of porous media. Phys. Rev. B, 47:8565–8574, Apr 1993.
- [38] Housseem. Haddar, Jing-Rebecca. Li, and Simona. Schiavi. Understanding the time-dependent effective diffusion coefficient measured by diffusion mri: the intracellular case. SIAM Journal on Applied Mathematics, 78(2):774–800, 2018.

# Apparent diffusion coefficient measured by diffusion MRI of moving and deforming domains

Imen Mekkaoui, Jerome Pousin, Jan Hesthaven, Jing-Rebecca Li



We present a second order (in the diffusion-encoding gradient magnitude) signal perturbation model for diffusion MRI in moving and deforming domains

- The linear term gives the imaginary part of the diffusion MRI signal;
- The quadratic term gives the apparent diffusion coefficient ;
- The scale of interest is that of a biological cell;
- The model is relevant to cardiac diffusion MRI;